Structure

Article

Complementary structures of the yeast phosphate transporter Pho90 provide insights into its transport mechanism

Graphical abstract

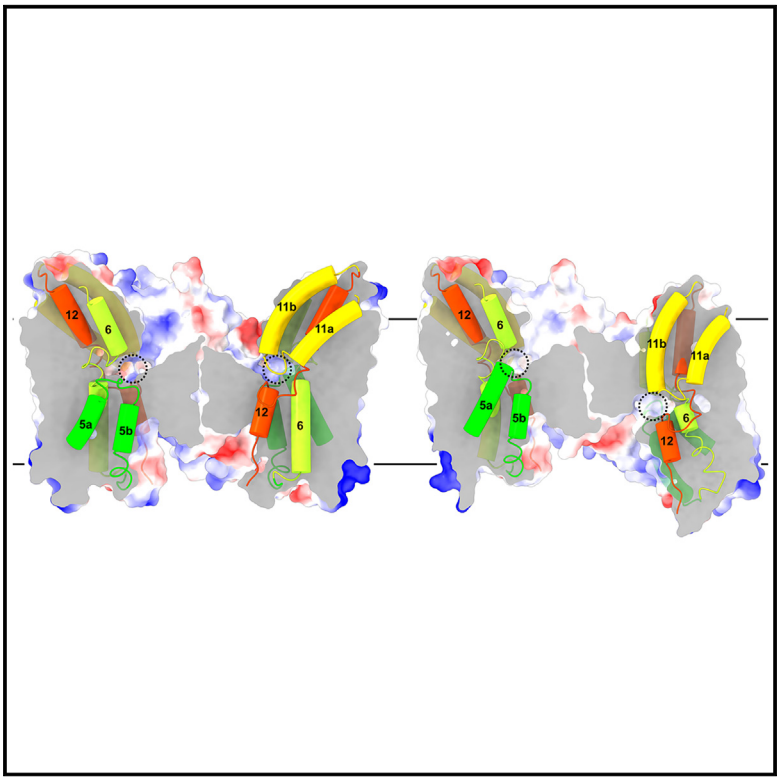

Authors

Simon Schneider, Werner Kühlbrandt, Özkan Yildiz

Correspondence

Oezkan.Yildiz@biophys.mpg.de

In brief

Schneider et al. report the cryo-EM structures of the yeast phosphate importer ScPho90 in different conformations, revealing insights into the phosphate transport mechanism by a low-affinity transporter.

Highlights

- Cryo-EM structures of the yeast low-affinity phosphate importer ScPho90
- Complementary structures reveal insights into the substrate translocation mechanism
- Comparisons with homologous transporters highlight the conserved transport mechanism
- Regulation by the SPX domain is discussed

Schneider et al., 2024, Structure *32*, 1–10
July 11, 2024
https://doi.org/10.1016/j.str.2024.04.005

CellPress

Please cite this article in press as: Schneider et al., Complementary structures of the yeast phosphate transporter Pho90 provide insights into its transport mechanism, Structure (2024), https://doi.org/10.1016/j.str.2024.04.005

Structure

CellPress

Article

Complementary structures of the yeast phosphate transporter Pho90 provide insights into its transport mechanism

Simon Schneider,[1] Werner Kühlbrandt,[1] and Özkan Yildiz[1,2,3,*]
[1]Department of Structural Biology, Max Planck Institute of Biophysics, 60438 Frankfurt am Main, Germany
[2]Structural Biology Unit, Max Planck Institute of Biophysics, 60438 Frankfurt am Main, Germany
[3]Lead contact
*Correspondence: Oezkan.Yildiz@biophys.mpg.de
https://doi.org/10.1016/j.str.2024.04.005

SUMMARY

Phosphate homeostasis is essential for all living organisms. Low-affinity phosphate transporters are involved in phosphate import and regulation in a range of eukaryotic organisms. We have determined the structures of the *Saccharomyces cerevisiae* phosphate importer Pho90 by electron cryomicroscopy in two complementary states at 2.3 and 3.1 Å resolution. The symmetrical, outward-open structure in the presence of phosphate indicates bound substrate ions in the binding pocket. In the absence of phosphate, Pho90 assumes an asymmetric structure with one monomer facing inward and one monomer facing outward, providing insights into the transport mechanism. The Pho90 transport domain binds phosphate ions on one side of the membrane, then flips to the other side where the substrate is released. Together with functional experiments, these complementary structures illustrate the transport mechanism of eukaryotic low-affinity phosphate transporters.

INTRODUCTION

Inorganic phosphate is an essential nutrient required by all living organisms in large quantities during growth and reproduction. The intracellular phosphate concentration is critical, as excess phosphate can impair cell metabolism and viability and must be tightly regulated.[1,2] For microorganisms and plants in particular, phosphate availability is often a main limiting factor for growth and proliferation.[3,4] Plants, fungi, and other organisms have developed effective mechanisms to regulate phosphate uptake and accumulation within the cell. In the budding yeast *Saccharomyces cerevisiae*, phosphate homeostasis is regulated by components of the phosphate signal transduction pathway,[5,6] which controls the accumulation, storage, recycling, and secretion of cellular phosphate.[7,8] Most of the genes encoding components of this pathway are regulated at transcriptional and post-transcriptional levels, depending on the intracellular phosphate concentration.[9]

Phosphate is accumulated by different types of phosphate importer proteins.[10] There are four different secondary-active phosphate importers in the plasma membrane of *S. cerevisiae* that transport phosphate from the cell exterior to the cytoplasm, classified as high-affinity and low-affinity transporters. *Sc*Pho84, a proton/phosphate symporter, and *Sc*Pho89, a sodium/phosphate symporter, are high-affinity transporters,[11,12] whereas *Sc*Pho87 and *Sc*Pho90 are low-affinity sodium/phosphate symporters.[10] Cooperation between the two types of uptake systems increases transport efficiency and ensures fast response to changing nutrient availability.[12] At low phosphate concentrations, the high-affinity phosphate transporters *Sc*Pho84 and *Sc*Pho89 are activated and responsible for raising intracellular phosphate levels.[13] Under these conditions, the low-affinity transporters are actively degraded and do not participate in phosphate uptake.[9] When the intracellular phosphate concentration reaches a sufficient level, the low-affinity phosphate transporters *Sc*Pho87 and *Sc*Pho90 are up-regulated to maintain a constant cytoplasmic phosphate concentration and prevent phosphate overload.[14,15] Simultaneously, high-affinity transporters are internalized and degraded.[16]

Sequence analysis indicates major differences in the structure, and therefore mechanism, of high- and low-affinity phosphate importers. So far, structural information is available only for homologs of *Sc*Pho84 and *Sc*Pho89,[17,18] while structures for low-affinity transporters have not been reported. The transmembrane regions of *Sc*Pho87 and *Sc*Pho90 show sequence homology to transporters of the divalent anion-sodium symporter (DASS) family, especially to the mammalian sodium sulfate symporters NaS1 (SLC13A1) and NaS2 (SLC13A4). *Sc*Pho87 and *Sc*Pho90 also have an N-terminal cytoplasmic domain that is found in a variety of proteins linked to phosphate homeostasis in yeast and plants.[7,8,19] This regulatory SPX domain derives its name from its presence in the Syg1, Pho, and Xpr1 proteins. The SPX domain has a characteristic three-helix bundle structure and is known to bind inositol-hexakisphosphate or its pyrophosphate

Please cite this article in press as: Schneider et al., Complementary structures of the yeast phosphate transporter Pho90 provide insights into its transport mechanism, Structure (2024), https://doi.org/10.1016/j.str.2024.04.005

variants.[20] The SPX domain of *Sc*Pho90 acts as a suppressor, as its deletion increases the phosphate uptake rate *in vivo*.[21] However, the mechanism by which the SPX domain interacts with the transmembrane region to regulate transport activity is unknown. *Sc*Pho87 and *Sc*Pho90 are sodium/phosphate symporters that use the sodium gradient to co-transport phosphate into the cell and share a sequence identity of 66%. Despite their high sequence identity, previous studies have shown that at high cellular phosphate concentrations, ScPho90 is the major phosphate transporter, whereas *Sc*Pho87 is mainly involved in phosphate sensing.[22] *Sc*Pho91, another phosphate transporter of *S. cerevisiae*, is a close homolog of *Sc*Pho87 and *Sc*Pho90 and is found in the vacuolar membrane. *Sc*Pho91 transports phosphate from the vacuole into the cytoplasm at low cytoplasmic phosphate levels.[23]

Here, we present structures of yeast *Sc*Pho90 in two different conformations determined by electron cryomicroscopy (cryo-EM), providing new insights into the mechanism by which the essential phosphate ions are transported through the membrane.

RESULTS

Cryo-EM structures of *Sc*Pho90 in presence and absence of phosphate

To investigate the molecular relationships of phosphate transport in dependence on its substrates in detail, we overexpressed *Sc*Pho90 in *S. cerevisiae* and purified it by affinity and size-exclusion chromatography (Figure S1A) for structure determination. Analysis of the purified protein by analytical size-exclusion chromatography, SDS-PAGE, and blue native PAGE indicates that *Sc*Pho90 is dimeric in detergent solution (Figures S1B and S1C). Negative-stain images of purified *Sc*Pho90 confirm a homogenous sample with particles of homogenous size (Figure S1D). Structures of *Sc*Pho90 were determined by cryo-EM in the presence or absence of phosphate. In total, 4,942 movies were recorded for *Sc*Pho90 with added phosphate and were used to calculate a 2.6 Å map with C2 symmetry (Figure S2; Table 1). Using *Sc*Pho90 samples without phosphate, we recorded a total of 13,845 movies and calculated a C2 symmetrical map at 2.3 Å (Figure S3; Table 1). A detailed analysis of the 3D variability[24] without applied symmetry showed that ~90% of the particles contribute to the symmetrical *Sc*Pho90 dimer map, while the other remaining 10% resulted in an asymmetrical map that was refined to a resolution of 3.1 Å (Figure S4; Table 1). Apart from the higher resolution, the symmetrical maps showed no recognizable overall differences (Figure S5A).

We built *ab initio* dimer models of *Sc*Pho90 into the maps (Figure 1). In total, each *Sc*Pho90 protomer has 13 helical elements (H1–H13) spanning the membrane. Seven are straight transmembrane helices (TMHs), four have unwound stretches within the membrane, and two are helix hairpins (H5, H11). The transmembrane part of *Sc*Pho90 dimers has a length of 90 Å, a width of 40 Å, and a height of 60 Å to just slightly protrude from the membrane on both sides (Figure 1). Helices H2–H7 and H8–H13 are organized in two inverted repeats connected by a cytoplasmic loop. The N terminus of helix H1 is on the cytoplasmic side while the C terminus of H13 points to the extracellular side. The cytoplasmic SPX domain is linked to the N terminus of H1 but due to its flexibility relative to the membrane domain, it is not highly resolved (Figures S2–S4).

The protomers dimerize through extensive hydrophobic interactions of seven helices (H1–4 and H8–10) in the scaffold domain of each protomer (Figures 1 and S6). Here, two tryptophans (Trp721 and Trp498) stand out in the unwound stretch of H4 and H10 of each protomer, which stabilize the dimer by π-stacking in the membrane center (Figures S6A and S6B). The other six TMHs (H5–7, H11–13), including the two helix hairpins (H5A/B and H11 A/B) and the two TMHs with unwound stretches (H6A/B and H12 A/B), form the transport domain as a helix bundle on either side of the central scaffold (Figure 2A). The scaffold and transport domains interact with each other mainly through hydrophobic interactions between H2, H4, H8, and H10 of the scaffold domain and H5, H6, H11, and H12 of the transport domain. In addition, both domains are linked by a salt bridge between Glu455 and Arg480 (Figure 2C).

The symmetrical dimers of *Sc*Pho90 with or without phosphate have virtually identical structures (Figure S5). Comparison of the protomers shows a root-mean-square deviation (RMSD) of 0.43 Å, whereas the protomers of the asymmetrical dimer without phosphate differ significantly with an RMSD of 7.8 Å (Figures 2B and S7). The main difference results from the position of the transport domain. In one protomer of the asymmetrical dimer, it protrudes into the extracellular space, while in the other protomer it extends into the cytoplasm through an 11 Å domain movement relative to the scaffold domain (Figure 2, Videos S1 and S2). The relative positions of the helices within the transport domain in the two protomers of the asymmetric dimer are essentially unchanged, indicating that the bundle moves as a rigid body from one position to the other. The interface between scaffold and transport domains in the inward-open protomer of the asymmetrical *Sc*Pho90 dimer is still hydrophobic, but the interacting side chains provided by the transport domain have changed position. Similarly, the ion bridge between Glu455 of the scaffold and Arg480 of the transport domain that is present in the outward-open conformation is replaced by an ion bridge between Glu688 and Lys614 in the inward-open conformation (Figure 2C).

Substrate binding pocket

The substrate binding pocket of *Sc*Pho90 is defined by the hairpin tips of helices H5 and H11 and by the unwound stretches of helices H6 and H12 (Figure 3). In contrast to other phosphate transporters with known structures[17,18] where the substrate binding site includes charged residues, only hydrophilic residues form the substrate binding pocket in *Sc*Pho90. In the map of *Sc*Pho90 with phosphate, we observed density in the substrate binding pocket that we interpreted as phosphate and sodium ions (Figure 3B). The phosphate ion is directly coordinated by the side chains of Asn556, Gln605, His779, and Ser815 and flanked by two sodium ions on both sides of the phosphate. In the first substrate binding site (Na1), the sodium ion is coordinated by the side chains of Ser603, Asn606, and Ser815 and by the main chain of Ala811. In the second site (Na2), the main-chain oxygens of Thr775, Gly817, and Leu820 and the side chain of Thr775 coordinate the sodium ion. Ser815 is the only residue involved in both phosphate and sodium ion

Please cite this article in press as: Schneider et al., Complementary structures of the yeast phosphate transporter Pho90 provide insights into its transport mechanism, Structure (2024), https://doi.org/10.1016/j.str.2024.04.005

Table 1. Data collection, processing, and refinement statistics

	ScPho90 with phosphate	ScPho90 phosphate-free symmetric	ScPho90 phosphate-free asymmetric
EMDB-ID	EMD-18860	EMD-18859	EMD-18861
PDB-ID	8R34	8R33	8R35
Data collection			
Microscope	Titan Krios G4i	Titan Krios G4i	
Detector	Falcon4	Falcon4	
Magnification	165,000	165,000	
Voltage (kV)	300	300	
Electron dose (e^{-}/Å^2)	65	70	
Defocus range (μm)	−0.6 to −2.2	−0.5 to −2.1	
Pixel size (Å)	0.573	0.573	
Movies	4,942	13,845	
Initial particles	476,290	1,857,014	
Final particles	192,548	304,932	33,833
Symmetry	C2	C2	C1
Map resolution (Å)	2.62	2.29	3.15
FSC threshold	0.143	0.143	0.143
Refinement			
Map sharpening B-factor (Å^2)	106.8	79.7	92.0
Model composition			
Non-hydrogen atoms	7,683	7,626	7,144
Protein residues	971	974	953
Ligands	14	12	0
B factors (Å^2)			
Protein	22.05	14.88	41.49
Ligand	25.59	18.04	–
Rms deviations			
Bond lengths (Å)	0.004	0.003	0.004
Bond angles (°)	0.645	0.589	0.723
Validation			
MolProbity score	1.96	1.68	1.76
Clash score	9.53	7.57	10.31
Poor rotamers (%)	2.65	2.14	0
Ramachandran plot			
Favored (%)	97.31	97.94	96.52
Allowed (%)	2.59	2.06	3.37
Disallowed (%)	0.10	0	0.11
Model refinement			
Model resolution (Å)	2.6	2.3	3.1

coordination. The binding pocket is accessible from the extracellular side and the phosphate-binding affinity *in vitro* was 1.9 ± 0.4 mM (Figure 3C). In the symmetrical structure without added phosphate, the density map indicates that the phosphate site is either empty or occupied by sodium ions or water molecules and that the side chains involved in phosphate-coordinating have to some extent changed conformation (Figure 3D).

SPX domain

Due to the flexible connection of the N-terminal regulatory SPX domain to the first TMH, the resolution in this region is not sufficient for secondary structure assignment (Figures S2–S4). A short part of the linker (Val377-Pro388 and Asn402-Lys407) connecting transmembrane and SPX domain is well resolved and forms a short beta-turn motif (Figures 1C, S6E, and S6F). The beta-turn is amphipathic with hydrophobic residues oriented toward the membrane and hydrophilic residues that point to the cytosol. Comparing the low-resolution density for the regulatory SPX domain with the predicted AlphaFold[25] model shows differences in its relative orientation to the transmembrane (TM) part of *Sc*Pho90 (Figure S9).

Please cite this article in press as: Schneider et al., Complementary structures of the yeast phosphate transporter Pho90 provide insights into its transport mechanism, Structure (2024), https://doi.org/10.1016/j.str.2024.04.005

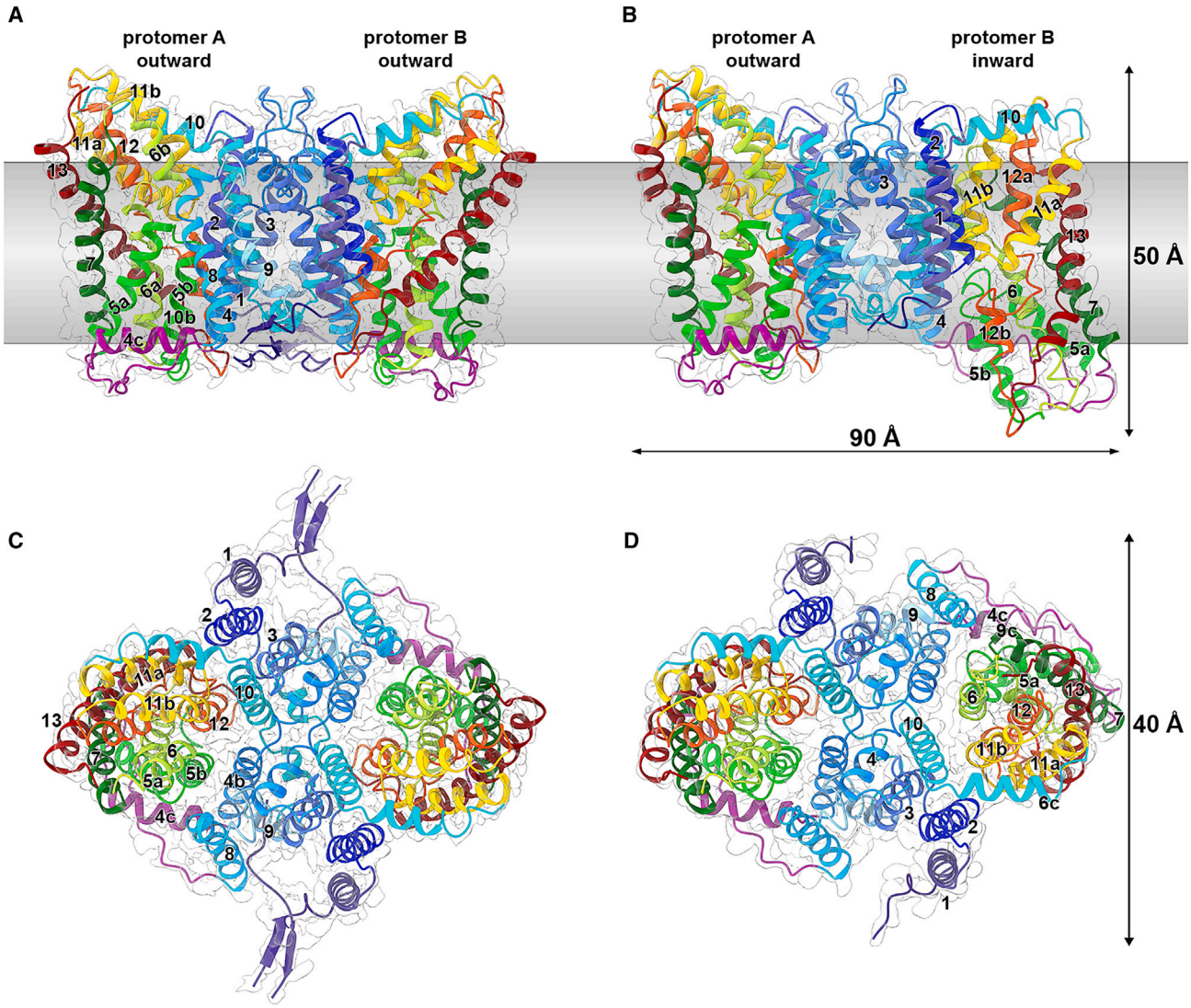

Figure 1. Cryo-EM structures of *Sc*Pho90 in two different conformations

Overview of the *Sc*Pho90 dimer structure in two different conformations seen along the membrane plane (A, B) and from the cytoplasmic side (C, D). The cryo-EM maps are shown in transparent gray and the model is colored by its individual helices. In the presence of phosphate, both *Sc*Pho90 protomers adopt a symmetrical, outward-open conformation with an overall map resolution of 2.6 Å (A, C). In the absence of phosphate, a fraction of the particles adopts an asymmetrical structure with one protomer in an inward-open conformation, the other in the outward-facing conformation, at an overall map resolution of 3.2 Å (B, D). The lipid bilayer is indicated in gray.

Role of lipids

In all our maps, we observed several lipid densities surrounding predominantly the scaffold domain. Several different types of lipids and sterols were identified by thin-layer chromatography (Figure S6C). Since the densities of lipid head groups were not well resolved, specific lipids could not be fitted with confidence and were instead modeled as phosphatidic acid (Figure S6D). Their binding sites at the transporter periphery suggest that their main role is to stabilize the dimer.

Functional characterization of *Sc*Pho90

For functional characterization of *Sc*Pho90, we reconstituted the transporter into liposomes and measured the transport activity. *Sc*Pho90 transports phosphate only in the presence of a sodium gradient across the liposome membrane (Figure 2D). To verify the role of Asn556 and Ser815 that coordinate the phosphate in the *Sc*Pho90 binding pocket, we mutated these residues to alanine. Both variants showed a diminished phosphate transport rate compared to the *Sc*Pho90$_{WT}$ (40% for Asn556Ala, 50% for Ser815Ala), highlighting the importance of these residues for the proper function of the transporter. We also examined the role of the cytoplasmic SPX domain in *Sc*Pho90-mediated phosphate transport. For this, we constructed a *Sc*Pho90 variant lacking the SPX domain (*Sc*Pho90$_{\Delta SPX}$). In contrast to the binding pocket variants, the transport activity of *Sc*Pho90$_{\Delta SPX}$ was not significantly different from that of *Sc*Pho90$_{WT}$ under the tested *in vitro* conditions. The addition of equimolar sulfate did not change the phosphate transport rate, indicating that

Please cite this article in press as: Schneider et al., Complementary structures of the yeast phosphate transporter Pho90 provide insights into its transport mechanism, Structure (2024), https://doi.org/10.1016/j.str.2024.04.005

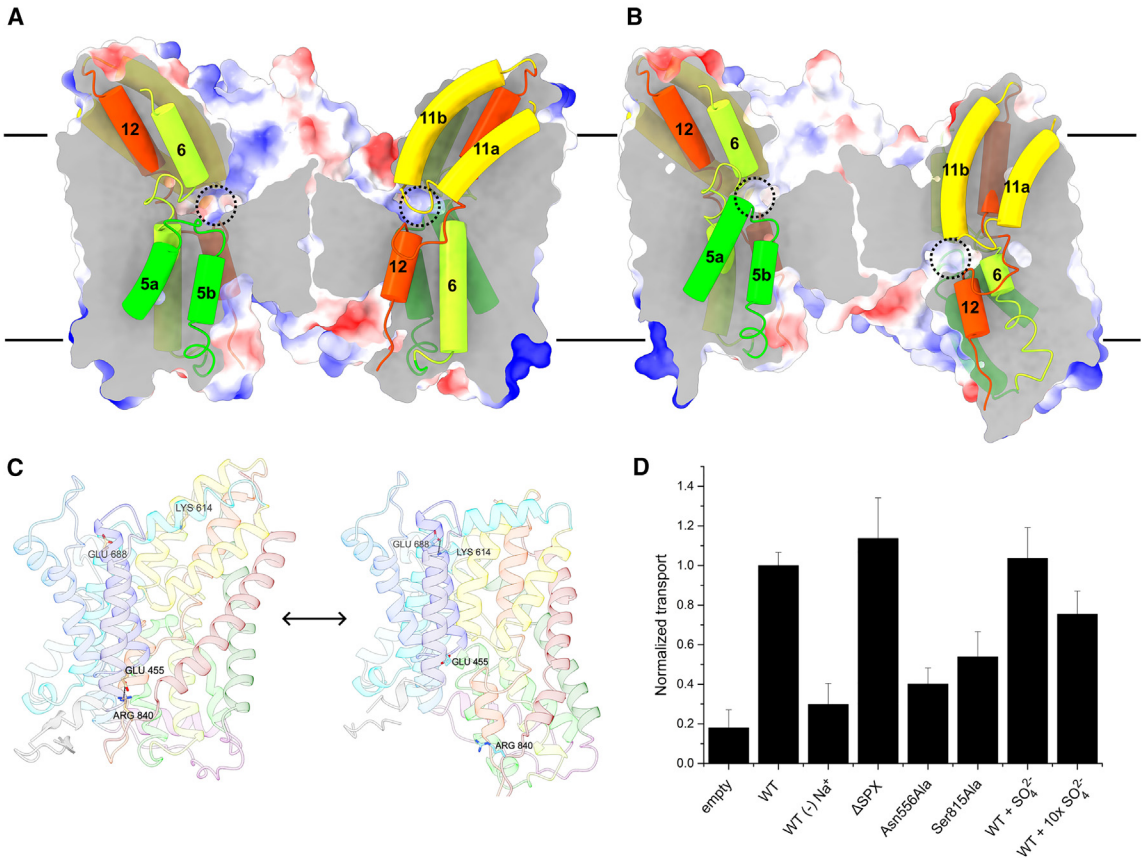

Figure 2. Conformational change and transport activities *Sc*Pho90

(A and B) Slices through *Sc*Pho90 in its two complementary conformations. The putative substrate binding pockets are indicated by dashed black circles and helices involved in the formation of the binding pocket are presented as tubes. The transport domain moves by ~11 Å.

(C) Salt bridges between scaffold and transport domain in the outward-open (left) and inward-open conformation (right).

(D) Phosphate transport into liposomes by wild-type *Sc*Pho90 and selected mutants. Transport rates are normalized to $ScPho90_{WT}$. Empty liposomes and liposomes without a sodium gradient show negligible transport. The deletion of the SPX domain (ΔSPX) has no effect on the transport rate, while the point mutations Asn556Ala and Ser815Ala reduce transport. Data are represented as mean ± SD (n = 3).

*Sc*Pho90 clearly prefers phosphate as a substrate. A 10-fold increase in sulfate concentration resulted in a slightly decreased transport rate (75% of $ScPho90_{WT}$), indicating a competitive effect of sulfate at elevated concentrations.

DISCUSSION

We present the high-resolution cryo-EM structures of *Sc*Pho90, a low-affinity phosphate transporter from *S. cerevisiae* that imports inorganic phosphate into the cell. The structures were obtained in presence or absence of phosphate and show substrate-dependent conformational changes that allowed us to build a complete atomic model of the transporter in its main conformational states. The overall dimeric fold of *Sc*Pho90 resembles that of transporters from the DASS family (Figure S10) such as *Hs*NaCT, *Vc*INDY, and *La*INDY.[26–29] Comparison of *Sc*Pho90 in an outward-open conformation with the *La*INDY structure in the same conformation reveals a conserved overall architecture (Figure 4A). Slight differences are observed in individual helix positions and loop regions. Similarly, comparison of *Sc*Pho90 in an inward-open conformation with *Vc*INDY and *Hs*NaCT structures in the same conformation also shows a conserved helix arrangement, with only marginal differences in individual helix positions (Figure 4B). This indicates a highly conserved translocation mechanism among the DASS family transporters.

In the presence of phosphate, both *Sc*Pho90 monomers assumed an outward-open conformation, in accordance with phosphate binding to the extracellular side and its translocation to the cytosol at sufficiently high phosphate concentration.[5] Due to the absence of a sodium gradient in the detergent-purified sample, the transporter is probably fixed in this conformation, as the conformational change cannot be energetically driven. Under these conditions, density for one bound phosphate and two sodium ions were observed in the binding pockets. The phosphate-coordinating residues are highly conserved in fungal low-affinity transporters Pho87, Pho90, and Pho91 (Figure S8), highlighting their importance for phosphate uptake, as confirmed by our transport measurements. Moreover, phosphate-coordinating motifs are related to the conserved SNT (Ser-Asn-Thr) motifs, which are involved in substrate binding in the *Hs*NaCT and INDY proteins.[26–29] In *Sc*Pho90, these motifs

Please cite this article in press as: Schneider et al., Complementary structures of the yeast phosphate transporter Pho90 provide insights into its transport mechanism, Structure (2024), https://doi.org/10.1016/j.str.2024.04.005

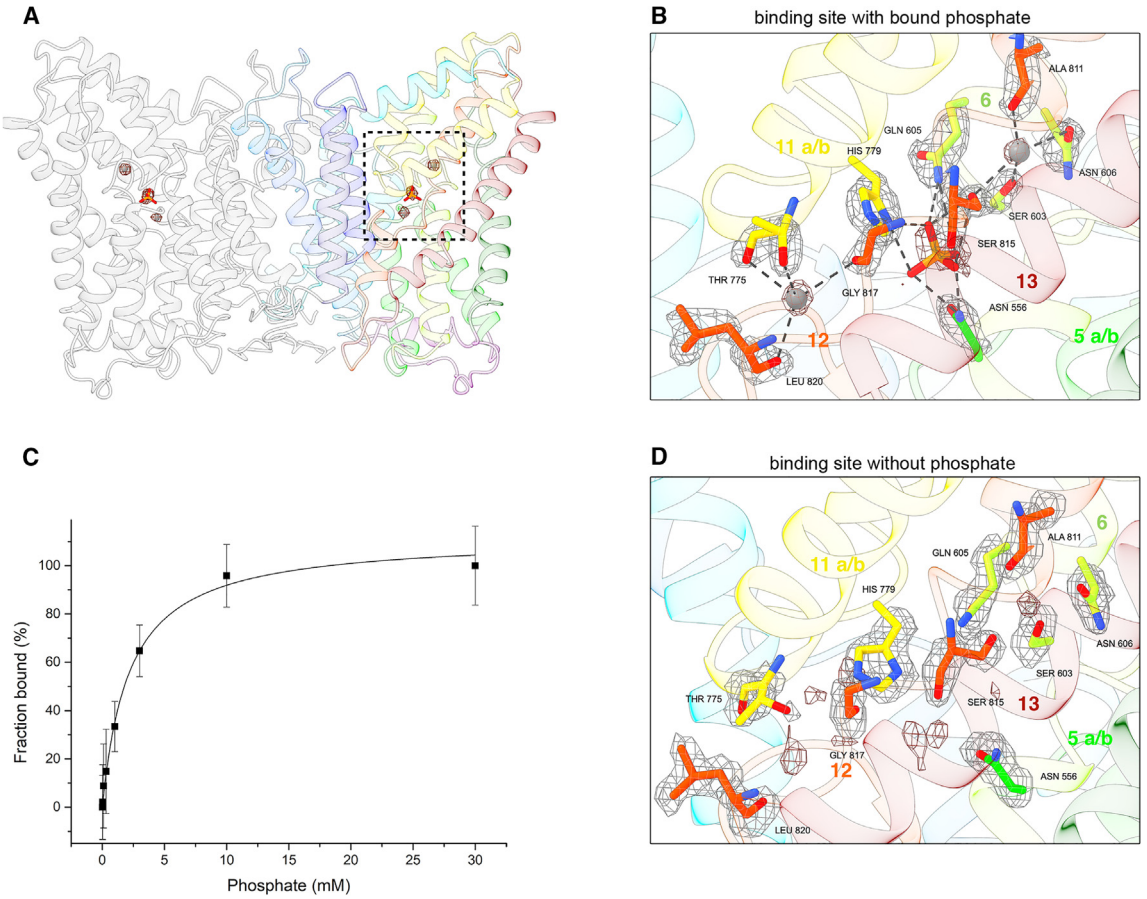

Figure 3. Substrate binding sites within the binding cavity

(A) Overview of phosphate and sodium binding sites of *Sc*Pho90. Map density is shown for bound substrate. The dashed box indicates the phosphate binding site.

Detailed view of phosphate and Na^+ coordinating residues in the presence (B) and absence (D) of phosphate. Map density around residues is shown as gray mesh and around substrates as light red mesh.

Phosphate binding affinity of purified *Sc*Pho90 (C) was determined by microscale thermophoresis resulting in a K_d value of 1.9 ± 0.4 mM. Data are represented as mean ± SD (n = 3).

consist of Ser555-Asn556-Val557 and Ser778-His779-Thr570, with Asn556 and His779 directly involved in phosphate binding. Comparing the substrate binding site in *Sc*Pho90 with those of *Vc*INDY and *Sc*Pho90 reveals that substrates are bound in similar positions, with the phosphate ion in *Sc*Pho90 being located deeper inside the transport domain (Figure 4C). This is likely due to the smaller size of phosphate compared to the di- and tricarboxylates in *Vc*INDY and *Hs*NaCT, enabling phosphate to bind more deeply in the binding pocket. The two bound sodium ions are located within the binding pocket but they are not in direct contact with the phosphate ion. A similar arrangement has been seen in other transporters of the DASS family,[26–29] although the exact position of the sodium ions differed (Figure 4C). It has also been demonstrated that *Vc*INDY and *Hs*NaCT likely couple substrate translocation to the transport of 3 or 4 sodium ions, even though only two sodium binding sites have been found.[30,31] We did not detect any other sodium ions in our structure. Additional studies are necessary to elucidate the substrate ratio for *Sc*Pho90 to possibly identify additional sodium binding sites.

The closest human homologs of *Sc*Pho90 are the sodium/sulfate co-transporter NaS1 and NaS2. Sequence alignment revealed that most of the phosphate-coordinating residues in these transporters are either conserved or replaced by functionally equivalent amino acids (Figure S8). As shown by our transport measurements, *Sc*Pho90 clearly favors phosphate over sulfate as a substrate. Previous comparison of high-affinity phosphate and sulfate-binding proteins has concluded that a charged residue, acting as hydrogen bond acceptor in the substrate binding site, is important for phosphate specificity.[32] However, there is no such residue within the binding site of ScPho90. In contrast, other phosphate transporters contain charged hydrogen bond acceptors that are involved in phosphate coordination.[17,18] This may explain the low substrate affinity of this phosphate transporter class, but the reason for its high substrate specificity remains elusive.

Please cite this article in press as: Schneider et al., Complementary structures of the yeast phosphate transporter Pho90 provide insights into its transport mechanism, Structure (2024), https://doi.org/10.1016/j.str.2024.04.005

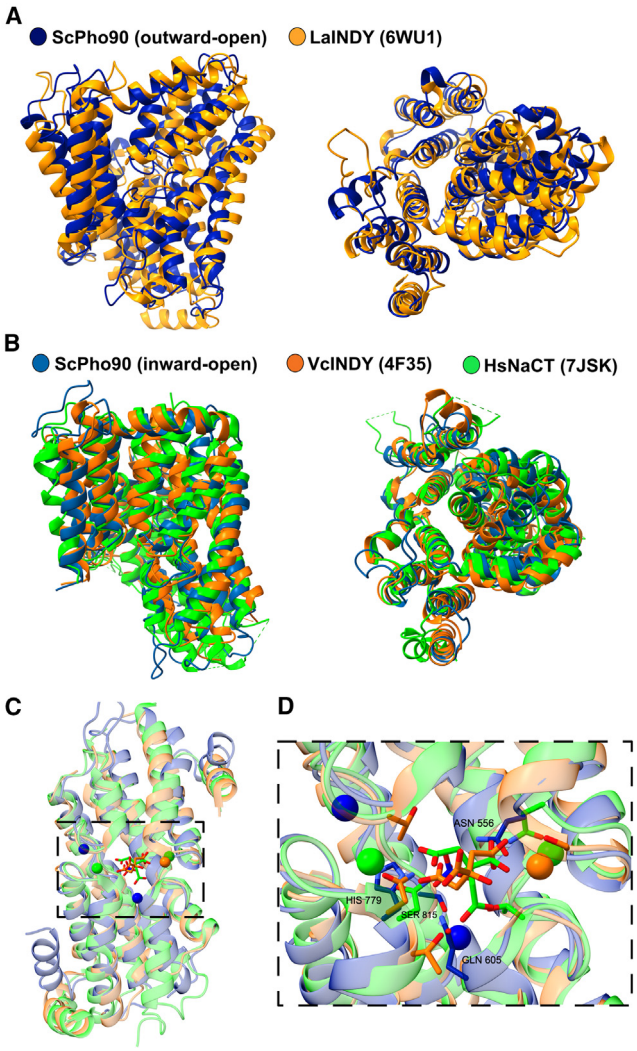

Figure 4. Comparison of *Sc*Pho90 with known structures of the DASS family

(A) Comparison of the *Sc*Pho90 monomer in the outward-open conformation with the *La*INDY structure as seen along the membrane plane and from the cytoplasmic side. The positions of individual helices vary slightly but the overall conformation is maintained.

(B) A comparison of the ScPho90 monomer in an inward-open conformation with *Vc*INDY and *Hs*NaCT structures indicates a conserved overall architecture with minor differences in individual helix positions.

(C) Superimposing the transport domains of ScPho90, *Vc*INDY, and *Hs*NaCT highlights differences in substrate binding sites. The positions of identified sodium ions (spheres) within the substrate binding pocket differ. Phosphate (*Sc*Pho90) and citrate ions (*Vc*INDY and *Hs*NaCT) are bound in similar positions but the phosphate ion is buried more deeply within the transport domain.

(D) Detailed view of residues involved in phosphate or citrate coordination (*Sc*Pho90 residues are labeled).

Variations within the substrate binding pockets between *Sc*Pho90 and NaS1/NaS2 might explain the difference in substrate specificity (Gln605 is replaced by a threonine and His779 is replaced by an asparagine in both human NaS1 and NaS2). However, the atomic basis for this difference in specificity needs further structural investigation.

Due to its homology to human NaS1 and NaS2, *Sc*Pho90 serves as a model for these transporters, for which there are so far no structures available. Defects in genes encoding NaS1 and NaS2 are linked to diseases related to defective sulfate homeostasis.[33–35]

The asymmetrical structure of *Sc*Pho90 in the absence of phosphate revealed two distinct conformations of the protein in the same dimer, whereby one monomer assumes the inside-open and the other one the outward-open state. These two conformations revealed insights into the phosphate transport mechanism: In the outward-open state, phosphate and sodium ions bind to the transport domain of *Sc*Pho90. This enables the movement of the binding pocket from the exterior toward the cytoplasm through a rigid-body movement of the transport domain helix bundle (Videos S1 and S2). In the inward-open state, the binding pocket is exposed to the cytoplasm, allowing phosphate and sodium to leave. This movement is energetically driven by the inward-directed sodium gradient, consistent with our transport measurements (Figure 2D). The overall energy barrier for the transition is unlikely to be high because the interactions between scaffold and transport domain in both conformations consist mainly of unspecific hydrophobic interactions covering a similar contact area. The sole broken salt bridge (Glu455-Arg480) is compensated by the formation of a new one (Glu688-Lys614) in the inward-open conformation (Figure 2C). We observe ordered lipid densities in the scaffold domain of the transporter (Figure S6C). These lipids might stabilize the scaffold domain, while less-ordered lipids in the transport domain may help to lower the energy barrier for the conformational change, which is necessary for the transport. During the transport domain movement, the spatial arrangement of the coordinating residues within the binding pocket changes slightly (Video S2), which may result in a decreased affinity for the substrates and its release into the cytoplasm. The substrate release then probably enables the conformational change back into the outward-open conformation.

The observation of both conformations in the same dimer is interesting, since it might indicate that the two protomers are not cooperative. This has also been proposed for *Vc*INDY and CitS.[27,36] However, other elevator-type transporters have been shown to exhibit positive or negative cooperativity.[37] Furthermore, since the different conformations are observed in the absence of phosphate, it is tempting to speculate that *Sc*Pho90 can transition between inward- and outward-open conformations in the absence of phosphate. However, this would potentially result in futile "slippage" cycles and dissipation of the sodium gradient, which we regard as unlikely under physiological conditions. How slippage is minimized while transport efficiency is maintained needs to be further investigated, as does the mode of cooperativity.

We observed an additional β-turn between the cytoplasmic SPX domain and the TM region. The function of this amphipathic stretch that would be located just below the membrane surface is so far unknown. Based on its position connecting the regulatory SPX and the transporter bundle, we can speculate that it might be involved in transducing regulatory signals from the SPX domain to the transporting TM part. The resolution of the SPX domain itself is not good enough for building

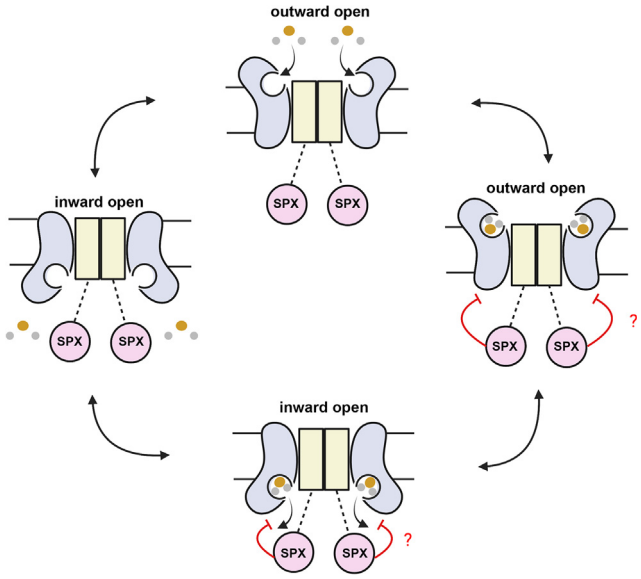

Figure 5. Substrate translocation mechanism and its possible regulation by the SPX domain

Schematic overview of different states during the *Sc*Pho90 phosphate transport cycle. In the outward-open conformation, phosphate (orange) and sodium ions (gray) can access the binding pocket of the transport domain (light blue) from the extracellular side. The scaffold domain is shown in light yellow. Upon substrate binding, the transport domain moves toward the cytoplasm resulting in an inward-open conformation and the accessibility of the binding pocket from the cytoplasm. Substrates are released into the cytoplasm which in turn could trigger the movement of the transporter back into an outward-open conformation. Regulation by the SPX domain (pink) might either inhibit the conformational change needed for substrate translocation or inhibit substrate release directly (Figure created with BioRender.com).

an atomic model. The lower resolution most likely results from the structural flexibility of the connecting linker between the scaffold domain and the SPX domain. Indeed, the structural flexibility of the linker is predicted by AlphaFold (Figure S9). The overall comparison of our maps and structures to the AlphaFold model shows a mismatch in the relative orientation of the SPX domain. This might be because the density represents an average of all orientations of the flexible SPX domain present in the transporter, while AlphaFold predicts a single conformation. Using 3D classification and 3D variability analysis, we were unable to determine discrete states of the SPX domain. Therefore, how the SPX domain regulates the *Sc*Pho90-catalyzed phosphate transport has to remain speculative. Deletion of the SPX domain revealed no significant impact in our *in vitro* phosphate transport assays. Previous *in vivo* studies however indicated an inhibitory effect of the SPX domain on phosphate transport.[21] These point to factors, which are absent in our *in vitro* reconstitutions, that may influence the regulatory function of the SPX domain. SPX domains are known to bind inositol pyrophosphates and it has been shown that they interact with soluble proteins such as Spl2 that might affect transport activity.[20,21]

Based on our structures and functional studies, we propose a model for the action of *Sc*Pho90-mediated phosphate transport (Figure 5). The general mechanism of substrate translocation concurs with previously described mechanisms of similar transporters.[26–29] Substrates bind to the transporter in the outward-open conformation, where the binding pocket is accessible from the extracellular side. Upon substrate binding, the transport domain moves relative to the scaffold domain by ~ 11 Å, resulting in an inward-open conformation. The binding pocket is then accessible from the cytoplasm and substrates can be released as a consequence of subtle rearrangements of coordinating residues and low intracellular sodium concentrations. The substrate-free transporter then changes its conformation back to the outward-open state, where it binds substrates and the cycle repeats.

The regulation of ScPho90 by its SPX domain most likely depends on additional intracellular factors including inositol pyrophosphates.[20,21] We speculate that upon interaction with these additional partners, the SPX domain either inhibits the conformational change or substrate release, thereby reducing the phosphate translocation rate (Figure 5). Additional structural and functional studies are needed to explain the regulatory function of the SPX domain, but the general transport mechanism of low-affinity phosphate transporter is now clear.

STAR★METHODS

Detailed methods are provided in the online version of this paper and include the following:

- KEY RESOURCES TABLE
- RESOURCE AVAILABILITY
  - Lead contact
  - Materials availability
  - Data and code availability
- EXPERIMENTAL MODEL AND STUDY PARTICIPANT DETAILS
  - Experimental model
  - Participant details
- METHOD DETAILS
  - Cloning, protein expression and purification
  - Cryo-EM grid preparation and data collection
  - Cryo-EM image processing
  - Model building and model interpretation
  - Reconstitution of ScPho90 into liposomes
  - Transport assay
  - Thin-layer chromatography
  - Microscale thermophoresis
  - Negative-stain grid preparation and imaging
- QUANTIFICATION AND STATISTICAL ANALYSIS

SUPPLEMENTAL INFORMATION

Supplemental information can be found online at https://doi.org/10.1016/j.str.2024.04.005.

ACKNOWLEDGMENTS

We thank Sabine Häder for experimental assistance, Susann Kaltwasser, Sonja Welsch, Simone Prinz, and Mark Linder at the Central Electron Microscopy of Max Planck Institute of Biophysics for electron microscopy training and assistance with cryo-EM data acquisition. We also thank Martin Centola for valuable discussions on cryo-EM data processing.

This work was funded by the Max Planck Society.

AUTHOR CONTRIBUTIONS

S.S. and Ö.Y. created the general concept and initiated the project. S.S. cloned, expressed, purified, and analyzed ScPho90, designed and performed

the biochemical activity measurements, prepared cryo-EM specimens, collected data, performed image analysis, and drafted the manuscript. Ö.Y. supervised the project. S.S. and Ö.Y. analyzed data. S.S., W.K., and Ö.Y. wrote and revised the manuscript.

DECLARATION OF INTERESTS

The authors declare no competing interests.

Received: November 17, 2023
Revised: March 1, 2024
Accepted: April 3, 2024
Published: April 29, 2024

REFERENCES

1. He, P., Mann-Collura, O., Fling, J., Edara, N., Hetz, R., and Razzaque, M.S. (2021). High phosphate actively induces cytotoxicity by rewiring pro-survival and pro-apoptotic signaling networks in HEK293 and HeLa cells. FASEB J. *35*, e20997. https://doi.org/10.1096/fj.202000799RR.
2. Yamada, S., Tokumoto, M., Tatsumoto, N., Taniguchi, M., Noguchi, H., Nakano, T., Masutani, K., Ooboshi, H., Tsuruya, K., and Kitazono, T. (2014). Phosphate overload directly induces systemic inflammation and malnutrition as well as vascular calcification in uremia. Am. J. Physiol. Ren. Physiol. *306*, F1418–F1428. https://doi.org/10.1152/ajprenal.00633.2013.
3. Vicent, I., Navarro, A., Mulet, J.M., Sharma, S., and Serrano, R. (2015). Uptake of inorganic phosphate is a limiting factor for Saccharomyces cerevisiae during growth at low temperatures. FEMS Yeast Res. *15*, fov008. https://doi.org/10.1093/femsyr/fov008.
4. Cridland, C., and Gillaspy, G. (2020). Inositol Pyrophosphate Pathways and Mechanisms: What Can We Learn from Plants? Molecules *25*, 2789. https://doi.org/10.3390/molecules25122789.
5. Austin, S., and Mayer, A. (2020). Phosphate Homeostasis - A Vital Metabolic Equilibrium Maintained Through the INPHORS Signaling Pathway. Front. Microbiol. *11*, 1367. https://doi.org/10.3389/fmicb.2020.01367.
6. Persson, B.L., Lagerstedt, J.O., Pratt, J.R., Pattison-Granberg, J., Lundh, K., Shokrollahzadeh, S., and Lundh, F. (2003). Regulation of phosphate acquisition in Saccharomyces cerevisiae. Curr. Genet. *43*, 225–244. https://doi.org/10.1007/s00294-003-0400-9.
7. Secco, D., Wang, C., Shou, H., and Whelan, J. (2012). Phosphate homeostasis in the yeast Saccharomyces cerevisiae, the key role of the SPX domain-containing proteins. FEBS Lett. *586*, 289–295. https://doi.org/10.1016/j.febslet.2012.01.036.
8. Secco, D., Wang, C., Arpat, B.A., Wang, Z., Poirier, Y., Tyerman, S.D., Wu, P., Shou, H., and Whelan, J. (2012). The emerging importance of the SPX domain-containing proteins in phosphate homeostasis. New Phytol. *193*, 842–851. https://doi.org/10.1111/j.1469-8137.2011.04002.x.
9. Wykoff, D.D., Rizvi, A.H., Raser, J.M., Margolin, B., and O'Shea, E.K. (2007). Positive feedback regulates switching of phosphate transporters in S. cerevisiae. Mol. Cell *27*, 1005–1013. https://doi.org/10.1016/j.molcel.2007.07.022.
10. Wykoff, D.D., and O'Shea, E.K. (2001). Phosphate transport and sensing in Saccharomyces cerevisiae. Genetics *159*, 1491–1499. https://doi.org/10.1093/genetics/159.4.1491.
11. Bun-Ya, M., Nishimura, M., Harashima, S., and Oshima, Y. (1991). The PHO84 gene of Saccharomyces cerevisiae encodes an inorganic phosphate transporter. Mol. Cell Biol. *11*, 3229–3238. https://doi.org/10.1128/mcb.11.6.3229-3238.1991.
12. Levy, S., Kafri, M., Carmi, M., and Barkai, N. (2011). The competitive advantage of a dual-transporter system. Science *334*, 1408–1412. https://doi.org/10.1126/science.1207154.
13. Persson, B.L., Berhe, A., Fristedt, U., Martinez, P., Pattison, J., Petersson, J., and Weinander, R. (1998). Phosphate permeases of Saccharomyces cerevisiae. Biochim. Biophys. Acta *1365*, 23–30. https://doi.org/10.1016/s0005-2728(98)00037-1.
14. Auesukaree, C., Homma, T., Kaneko, Y., and Harashima, S. (2003). Transcriptional regulation of phosphate-responsive genes in low-affinity phosphate-transporter-defective mutants in Saccharomyces cerevisiae. Biochem. Biophys. Res. Commun. *306*, 843–850. https://doi.org/10.1016/s0006-291x(03)01068-4.
15. Tamai, Y., Toh-e, A., and Oshima, Y. (1985). Regulation of inorganic phosphate transport systems in Saccharomyces cerevisiae. J. Bacteriol. *164*, 964–968. https://doi.org/10.1128/jb.164.2.964-968.1985.
16. Lundh, F., Mouillon, J.M., Samyn, D., Stadler, K., Popova, Y., Lagerstedt, J.O., Thevelein, J.M., and Persson, B.L. (2009). Molecular mechanisms controlling phosphate-induced downregulation of the yeast Pho84 phosphate transporter. Biochemistry *48*, 4497–4505. https://doi.org/10.1021/bi9001198.
17. Tsai, J.Y., Chu, C.H., Lin, M.G., Chou, Y.H., Hong, R.Y., Yen, C.Y., Hsiao, C.D., and Sun, Y.J. (2020). Structure of the sodium-dependent phosphate transporter reveals insights into human solute carrier SLC20. Sci. Adv. *6*, eabb4024. https://doi.org/10.1126/sciadv.abb4024.
18. Pedersen, B.P., Kumar, H., Waight, A.B., Risenmay, A.J., Roe-Zurz, Z., Chau, B.H., Schlessinger, A., Bonomi, M., Harries, W., Sali, A., et al. (2013). Crystal structure of a eukaryotic phosphate transporter. Nature *496*, 533–536. https://doi.org/10.1038/nature12042.
19. Jung, J.Y., Ried, M.K., Hothorn, M., and Poirier, Y. (2018). Control of plant phosphate homeostasis by inositol pyrophosphates and the SPX domain. Curr. Opin. Biotechnol. *49*, 156–162. https://doi.org/10.1016/j.copbio.2017.08.012.
20. Wild, R., Gerasimaite, R., Jung, J.Y., Truffault, V., Pavlovic, I., Schmidt, A., Saiardi, A., Jessen, H.J., Poirier, Y., Hothorn, M., and Mayer, A. (2016). Control of eukaryotic phosphate homeostasis by inositol polyphosphate sensor domains. Science *352*, 986–990. https://doi.org/10.1126/science.aad9858.
21. Hürlimann, H.C., Pinson, B., Stadler-Waibel, M., Zeeman, S.C., and Freimoser, F.M. (2009). The SPX domain of the yeast low-affinity phosphate transporter Pho90 regulates transport activity. EMBO Rep. *10*, 1003–1008. https://doi.org/10.1038/embor.2009.105.
22. Ghillebert, R., Swinnen, E., De Snijder, P., Smets, B., and Winderickx, J. (2011). Differential roles for the low-affinity phosphate transporters Pho87 and Pho90 in Saccharomyces cerevisiae. Biochem. J. *434*, 243–251. https://doi.org/10.1042/BJ20101118.
23. Hürlimann, H.C., Stadler-Waibel, M., Werner, T.P., and Freimoser, F.M. (2007). Pho91 Is a vacuolar phosphate transporter that regulates phosphate and polyphosphate metabolism in Saccharomyces cerevisiae. Mol. Biol. Cell *18*, 4438–4445. https://doi.org/10.1091/mbc.e07-05-0457.
24. Punjani, A., Rubinstein, J.L., Fleet, D.J., and Brubaker, M.A. (2017). cryoSPARC: algorithms for rapid unsupervised cryo-EM structure determination. Nat. Methods *14*, 290–296. https://doi.org/10.1038/Nmeth.4169.
25. Jumper, J., Evans, R., Pritzel, A., Green, T., Figurnov, M., Ronneberger, O., Tunyasuvunakool, K., Bates, R., Žídek, A., Potapenko, A., et al. (2021). Highly accurate protein structure prediction with AlphaFold. Nature *596*, 583–589. https://doi.org/10.1038/s41586-021-03819-2.
26. Mancusso, R., Gregorio, G.G., Liu, Q., and Wang, D.N. (2012). Structure and mechanism of a bacterial sodium-dependent dicarboxylate transporter. Nature *491*, 622–626. https://doi.org/10.1038/nature11542.
27. Wöhlert, D., Grötzinger, M.J., Kühlbrandt, W., and Yildiz, Ö. (2015). Mechanism of Na(+)-dependent citrate transport from the structure of an asymmetrical CitS dimer. Elife *4*, e09375. https://doi.org/10.7554/eLife.09375.
28. Sauer, D.B., Song, J., Wang, B., Hilton, J.K., Karpowich, N.K., Mindell, J.A., Rice, W.J., and Wang, D.N. (2021). Structure and inhibition mechanism of the human citrate transporter NaCT. Nature *591*, 157–161. https://doi.org/10.1038/s41586-021-03230-x.

29. Sauer, D.B., Trebesch, N., Marden, J.J., Cocco, N., Song, J., Koide, A., Koide, S., Tajkhorshid, E., and Wang, D.N. (2020). Structural basis for the reaction cycle of DASS dicarboxylate transporters. Elife *9*, e61350. https://doi.org/10.7554/eLife.61350.

30. Fitzgerald, G.A., Mulligan, C., and Mindell, J.A. (2017). A general method for determining secondary active transporter substrate stoichiometry. Elife *6*, e21016. https://doi.org/10.7554/eLife.21016.

31. Inoue, K., Fei, Y.J., Zhuang, L., Gopal, E., Miyauchi, S., and Ganapathy, V. (2004). Functional features and genomic organization of mouse NaCT, a sodium-coupled transporter for tricarboxylic acid cycle intermediates. Biochem. J. *378*, 949–957. https://doi.org/10.1042/BJ20031261.

32. Quiocho, F.A. (1996). Atomic basis of the exquisite specificity of phosphate and sulfate transport receptors. Kidney Int. *49*, 943–946. https://doi.org/10.1038/ki.1996.132.

33. van de Kamp, J.M., Bökenkamp, A., Smith, D.E.C., Wamelink, M.M.C., Jansen, E.E.W., Struys, E.A., Waisfisz, Q., Verkleij, M., Hartmann, M.F., Wang, R., et al. (2023). Biallelic variants in the SLC13A1 sulfate transporter gene cause hyposulfatemia with a mild spondylo-epi-metaphyseal dysplasia. Clin. Genet. *103*, 45–52. https://doi.org/10.1111/cge.14239.

34. Rakoczy, J., Zhang, Z., Bowling, F.G., Dawson, P.A., and Simmons, D.G. (2015). Loss of the sulfate transporter Slc13a4 in placenta causes severe fetal abnormalities and death in mice. Cell Res. *25*, 1273–1276. https://doi.org/10.1038/cr.2015.100.

35. Bjornsdottir, G., Stefansdottir, L., Thorleifsson, G., Sulem, P., Norland, K., Ferkingstad, E., Oddsson, A., Zink, F., Lund, S.H., Nawaz, M.S., et al. (2022). Rare SLC13A1 variants associate with intervertebral disc disorder highlighting role of sulfate in disc pathology. Nat. Commun. *13*, 634. https://doi.org/10.1038/s41467-022-28167-1.

36. Kinz-Thompson, C., Lopez-Redondo, M.L., Mulligan, C., Sauer, D.B., Marden, J.J., Tajkhorshid, E., Hunt, J.F., Stokes, D.L., Mindell, J.A., Wang, D.N., and Gonzalez, R.L. (2023). Elevator mechanism dynamics in a sodium-coupled dicarboxylate transporter. Protein Sci. *32*.

37. Holzhüter, K., and Geertsma, E.R. (2020). Functional (un)cooperativity in elevator transport proteins. Biochem. Soc. Trans. *48*, 1047–1055. https://doi.org/10.1042/Bst20190970.

38. Parker, J.L., and Newstead, S. (2014). Method to increase the yield of eukaryotic membrane protein expression in Saccharomyces cerevisiae for structural and functional studies. Protein Sci. *23*, 1309–1314. https://doi.org/10.1002/pro.2507.

39. Scheres, S.H.W. (2012). A Bayesian view on cryo-EM structure determination. J. Mol. Biol. *415*, 406–418. https://doi.org/10.1016/j.jmb.2011.11.010.

40. Zhang, K. (2016). Gctf: Real-time CTF determination and correction. J. Struct. Biol. *193*, 1–12. https://doi.org/10.1016/j.jsb.2015.11.003.

41. Wagner, T., Merino, F., Stabrin, M., Moriya, T., Antoni, C., Apelbaum, A., Hagel, P., Sitsel, O., Raisch, T., Prumbaum, D., et al. (2019). SPHIRE-crYOLO is a fast and accurate fully automated particle picker for cryo-EM. Commun. Biol. *2*, 218. https://doi.org/10.1038/s42003-019-0437-z.

42. Adams, P.D., Afonine, P.V., Bunkóczi, G., Chen, V.B., Davis, I.W., Echols, N., Headd, J.J., Hung, L.W., Kapral, G.J., Grosse-Kunstleve, R.W., et al. (2010). PHENIX: a comprehensive Python-based system for macromolecular structure solution. Acta Crystallogr. D Biol. Crystallogr. *66*, 213–221. https://doi.org/10.1107/S0907444909052925.

43. Emsley, P., and Cowtan, K. (2004). Coot: model-building tools for molecular graphics. Acta Crystallogr. D Biol. Crystallogr. *60*, 2126–2132.

44. Goddard, T.D., Huang, C.C., Meng, E.C., Pettersen, E.F., Couch, G.S., Morris, J.H., and Ferrin, T.E. (2018). UCSF ChimeraX: Meeting modern challenges in visualization and analysis. Protein Sci. *27*, 14–25. https://doi.org/10.1002/pro.3235.

45. Gietz, R.D., and Schiestl, R.H. (2007). High-efficiency yeast transformation using the LiAc/SS carrier DNA/PEG method. Nat. Protoc. *2*, 31–34. https://doi.org/10.1038/nprot.2007.13.

46. Punjani, A., and Fleet, D.J. (2021). 3D variability analysis: Resolving continuous flexibility and discrete heterogeneity from single particle cryo-EM. J. Struct. Biol. *213*, 107702. https://doi.org/10.1016/j.jsb.2021.107702.

47. Terwilliger, T.C., Sobolev, O.V., Afonine, P.V., Adams, P.D., and Read, R.J. (2020). Density modification of cryo-EM maps. Acta Crystallogr. D Struct. Biol. *76*, 912–925. https://doi.org/10.1107/S205979832001061X.

48. Chen, V.B., Arendall, W.B., Headd, J.J., Keedy, D.A., Immormino, R.M., Kapral, G.J., Murray, L.W., Richardson, J.S., and Richardson, D.C. (2010). MolProbity: all-atom structure validation for macromolecular crystallography. Acta Crystallogr. D Biol. Crystallogr. *66*, 12–21. https://doi.org/10.1107/S0907444909042073.

49. Pettersen, E.F., Goddard, T.D., Huang, C.C., Couch, G.S., Greenblatt, D.M., Meng, E.C., and Ferrin, T.E. (2004). UCSF Chimera–a visualization system for exploratory research and analysis. J. Comput. Chem. *25*, 1605–1612. https://doi.org/10.1002/jcc.20084.

Please cite this article in press as: Schneider et al., Complementary structures of the yeast phosphate transporter Pho90 provide insights into its transport mechanism, Structure (2024), https://doi.org/10.1016/j.str.2024.04.005

STAR★METHODS

KEY RESOURCES TABLE

REAGENT or RESOURCE	SOURCE	IDENTIFIER
Bacterial and virus strains		
E. coli DH5α Genotype: F⁻ endA1 glnV44 thi-1 recA1 relA1 gyrA96 deoR nupG purB20 φ80dlacZδM15 δlacZYA-argF)U169, hsdR17 λ⁻.	ThermoFisher	ThermoFisher 18265017
Deposited data		
ScPho90 with phosphate model	This paper	PDB: 8R34
ScPho90 with phosphate map	This paper	EMDB: EMD-18860
ScPho90 phosphate-free symmetric model	This paper	PDB: 8R33
ScPho90 phosphate-free symmetric map	This paper	EMBD: EMD-18859
ScPho90 phosphate-free asymmetric model	This paper	PDB: 8R35
ScPho90 phosphate-free asymmetric map	This paper	EMBD: EMD-18861
Experimental models: Organisms/strains		
S. cerevisiae BJ5460 Genotype: MATa ura3-52 trp1 lys2-801 leu2-delta1 his3-delta200 pep4:HIS3 prb1-delta1.6R can1 GAL	ATCC	ATCC 208285
Oligonucleotides		
Primer ScPho90 NdeI fwd.: ctatcaCATATGcgtttttcccacttttgaag	This paper	N/A
Primer ScPho90 TMonly390- NdeI fwd.: agttatCATATGctgccgcgtccgattaacctgaaattcacc	This paper	N/A
Primer ScPho90 XhoI rev.: TGATATctcgagcgcagaggtcgcattgc	This paper	N/A
Primer ScPho90 N556A fwd.: ggatcagcGCTgttgcagcgccggtgctg	This paper	N/A
Primer ScPho90 N556A rev.: gcgctgcaacAGCgctgatccacatgctcagg	This paper	N/A
Primer ScPho90 T815A fwd.: gctgctgagcGCTtgtggtatgggtctggcgagc	This paper	N/A
Primer ScPho90 T815A rev.: ccataccacaAGCgctcagcagcgcgcaacc	This paper	N/A
Recombinant DNA		
pDD vector	Parker and Newstead[38]	Addgene Plasmid #6265
Software and algorithms		
RELION	Scheres[39]	https://github.com/3dem/relion
GCTF	Zhang[40]	https://www2.mrc-lmb.cam.ac.uk/download/gctf/
crYOLO	Wagner et al.[41]	https://cryolo.readthedocs.io/en/stable/
CryoSPARC	Punjani et al.[24]	https://cryosparc.com/
PHENIX	Adams et al.[42]	https://phenix-online.org/
Coot	Emsley and Cowtan[43]	https://www2.mrc-lmb.cam.ac.uk/personal/pemsley/coot/
ChimeraX	Goddard et al.[44]	https://www.cgl.ucsf.edu/chimerax/

RESOURCE AVAILABILITY

Lead contact

Further information and requests for resources and reagents should be directed to and will be fulfilled by the lead contact, Özkan Yildiz, (Oezkan.Yildiz@biophys.mpg.de).

Materials availability

All unique/stable reagents generated in this study are available from the lead contact with a completed Materials Transfer Agreement.

Data and code availability

- Cryo-EM maps and structure models are publicly available through the Electron Microscopy DataBank (EMDB) and Protein DataBank (PDB) databases. Structure model coordinates have been deposited in the PDB with the accession codes: PDB: 8R34 for the substrate-bound symmetric model of ScPho90, PDB: 8R33 for the symmetric model of ScPho90 in the absence of phosphate and PDB: 8R35 for the asymmetric model of ScPho90 in the absence of phosphate. Cryo-EM maps for ScPho90 are available under the accession codes EMDB: EMD-18860 for the symmetrized ScPho90 map in the presence of phosphate, EMDB: EMD-18859 for the symmetrized ScPho90 map in the absence of phosphate and EMDB: EMD-18861 for the asymmetric ScPho90 map in the absence of phosphate.
- This paper does not report original code.
- Any additional information required to reanalyze the data reported in this paper is available from the lead contact upon request.

EXPERIMENTAL MODEL AND STUDY PARTICIPANT DETAILS

Experimental model

In this study, *S. cerevisiae BJ5460* (ATCC 208285) was used as expression host. Genotype: MATa ura3-52 trp1 lys2-801 leu2-delta1 his3-delta200 pep4HIS3 prb1-delta1.6R can1 GAL.

In this study, *E. coli DH5α* (ThermoFisher 18265017) was used for subcloning of the expression vectors. Genotype: F^- endA1 glnV44 thi-1 recA1 relA1 gyrA96 deoR nupG purB20 φ80dlacZδM15 δlacZYA-argF)U169, hsdR17 λ^-.

Participant details

No other microbes, animals, plants, or humans have been used as models in this study.

METHOD DETAILS

Cloning, protein expression and purification

Synthetic gene encoding for Pho90 from *Saccharomyces cerevisiae* (ScPho90) with a thrombin-cleavable His_{10}-tag at the C-terminus was cloned into the *S. cerevisiae* expression vector pDD[38] that was used to transform competent *S. cerevisiae* BJ5460 (ATCC 208285) by the lithium-acetate method.[45] Transformed cells were selected on -URA synthetic dropout plates and a single clone was used to inoculate 10 mL of yeast drop-out medium (-URA). The culture was grown for 18 h at 30°C and was used as pre-culture to inoculate 1 L of yeast drop-out medium (-URA), which was incubated at 30°C for 24 h. 10 L of yeast drop-out expression medium (-URA) were inoculated with the previous culture and incubated at 30°C for 20h. Protein expression was induced by adding galactose at a final concentration of 2% at 25°C for 24h. Cells were collected by centrifugation at 7,500 g for 10 min at 4°C, resuspended in 50 mM KP_i pH 8.0, 100 mM NaCl, protease inhibitor cocktail (Roche), DNase, and broken with a cell disruptor (Constant System Ltd) at a pressure of 35 psi. Cell debris and unbroken cells were removed by centrifugation at 15,000 g for 30 min at 4°C.

Membrane fractions were pelleted by ultracentrifugation at 200,000 g for 75 min and resuspended in ice-cold 50 mM KP_i pH 8.0, 100 mM NaCl, 10% glycerol. Protein solubilization was achieved by the addition of 0.5% Lauryl Maltose Neopentyl Glycol (LMNG) and 0.05% Cholesterol hemisuccinate (CHS) and incubation for 2h. Insoluble material was discarded by ultracentrifugation at 150,000 g for 60 min. To the supernatant 20 mM imidazole was added, mixed with Ni-NTA (Sigma-Aldrich) and incubated for 1h at 4°C. The slurry was loaded to a gravity-flow column and washed with 10 CV 20 mM KP_i pH 8.0, 250 mM NaCl, 10% glycerol, 2 mM $MgSO_4$, 50 mM imidazole, 0.005%/0.0005% LMNG/CHS followed by 10 CV 20 mM KP_i pH 8.0, 100 mM NaCl, 2 mM $MgSO_4$, 10% glycerol, 0.005%/0.0005% LMNG/CHS. Bound protein was eluted with 3 CV 20 mM KP_i pH 8.0, 100 mM NaCl, 2 mM $MgSO_4$, 250 mM imidazole, 10% glycerol and concentrated to approx. 50 μL using an Amicon spin concentrator (100 kDa cut-off). The concentrated protein solution was applied to a Superdex 200 Inc. 5/150 size-exclusion column equilibrated with 20 mM KP_i pH 8.0, 100 mM NaCl, 0.005%/0.0005% LMNG/CHS. Elution fractions containing ScPho90 were pooled and used for subsequent experiments. To analyze the substrate-free structures of ScPho90, the phosphate buffer was exchanged for Tris-HCl pH 8.0 in all purification buffers.

Cryo-EM grid preparation and data collection

3 μL of ScPho90 at a concentration of 2.5 mg/mL were applied to freshly glow-discharged C-Flat 1.2/1.3 300 mesh Cu/C grids and plunge-frozen in liquid ethane using a Vitrobot Mk 4 (Thermo Scientific). Images were collected on a Krios G4 transmission electron microscope (Thermo Scientific), operated at 300kV in EFTEM mode and equipped with a SelectrisX energy filter (Slit width: 8 eV) and a Falcon4 camera operated in counting mode. Movies in EER format were collected at 215kx nominal magnification corresponding to a calibrated pixel size of 0.573 Å. The total dose per image was 65 $e^-/Å^2$ and the defocus ranged from −0.6 to −2.2 μm in the phosphate-bound dataset. The phosphate-free dataset was recorded with a total dose of 70 $e^-/Å^2$ and a defocus range from −0.5 to −2.1 μm.

Cryo-EM image processing

All collected movies were motion-corrected using the algorithm implemented in RELION,[39] and CTF was estimated with GCTF.[40] Motion-corrected micrographs were low-pass filtered to 10 Å for particle picking with crYOLO.[41] After training on manually picked

Please cite this article in press as: Schneider et al., Complementary structures of the yeast phosphate transporter Pho90 provide insights into its transport mechanism, Structure (2024), https://doi.org/10.1016/j.str.2024.04.005

particles from 30 micrographs, crYOLO picked a total of 1,865,366 particles that were extracted in RELION. Particle stacks were imported into CryoSPARC[24] and multiple rounds of 2D-classification were used to remove false-positive picks. Ab-initio reconstruction with multiple classes and subsequent heterogeneous refinement were applied to further homogenize the particle stacks. NU-refinement of the best class with imposed C2-symmetry yielded the final maps.

In the phosphate-free dataset, 3D variability analysis in CryoSPARC[24,46] revealed the transport motion of the transporter and displayed another confirmation of the protein. 3D classification was used to classify particles into the different confirmations. Particles classified into the asymmetric confirmation were further refined using NU-refinement and yielded the final map of the asymmetric structure.

The final symmetrical maps were density modified using the Phenix tool resolve_cryo_em.[47] The asymmetrical map was sharpened using CryoSPARC's implemented tool.

Model building and model interpretation

Initial models were obtained using Alphafold and individual domains were rigid body fitted into the density map and manually corrected in Coot.[43] Models were finalized by iterative manual model building in Coot and refinement against the full map using Phenix real-space-refinement.[42] Models were validated by MolProbity.[48] Table 1 summarizes data acquisition and refinement statistics. Figures were created with either ChimeraX[44] or Chimera.[49]

Reconstitution of ScPho90 into liposomes

A lipid mixture (55% POPC, 35% DOPE, 10% POPI) was mixed with 15% Ergosterol (w/w) in chloroform and dried under a gentle flow of nitrogen stream overnight. The dried lipids were resuspended in lipid buffer (20 mM Tris pH 8.0, 150 mM KCl) by sonication and heating. The lipid suspension was diluted to 5 mg/mL and freeze-thaw cycles were applied to produce unilammelar vesicles. The suspension was extruded through a 400 nm sized membrane to get liposomes with diameter of ~400 nm. The suspension was further diluted to 2.5 mg/mL and stored at −80°C until further use. For reconstitution liposomes were mixed with ScPho90 (purified in DDM/CHS) in a 50:1 ratio (w/w) and incubated for 30 min at room temperature, were supplemented with 80 mg Bio-beads and incubated at 4°C. After 1 h, another 80 mg fresh Bio-beads were added. On the next day another 100 mg Bio-beads were added and the mixture was incubated at room temperature for 2h. Proteoliposomes were flash-frozen in liquid nitrogen and stored at −80°C until further use.

Transport assay

Proteoliposomes were thawed and ultra-centrifuged for 30 min at 200,000 g. The supernatant was discarded and liposomes were resuspended in assay buffer (20 mM Tris pH 8.0, 150 mM NaCl or KCl) at a final lipid concentration of 2.0 mg/mL. Transport assays were started by adding 20 mM KP_i to 250 μL liposome suspension and incubated at 30°C for 30 min. Sulfate competition experiments were carried out with addition of 20 mM or 200 mM $MgSO_4$. After transport reactions liposomes were ultra-centrifuged for 30 min at 200,000 g, washed twice with assay buffer and ultra-centrifuged for 30 min at 200,000 g. Liposomes were resuspended in 25 μL assay buffer containing 0.5% SDS. The solution was mixed with 25 μL 40 mM H_2SO_4 and 25 μL malachite green solution (0.8 mg/mL malachite green, 15% H_2SO_4, 5% Na_2MnO_4) and incubated for 5 min. The absorbance of each sample was measured in a microwell plate at 620 nm using a SpectraMax M2 (Molecular Devices).

Thin-layer chromatography

50 μg of ScPho90 was precipitated in a 2:1 methanol:chloroform mixture. The mixture was spun down for 15 min at 4,000g to separate organic and aqueous phases. The organic phase was evaporated under nitrogen and the dried lipids were resuspended in 10 μL of chloroform. The sample and standards were applied to a silica plate which was put into a preequilibrated TLC chamber and run for approx. 25 min (Running buffer: 39 mL chloroform, 15 mL methanol, 2.4 mL water). The silica plate was dried and lipid bands were visualized using elemental iod.

Microscale thermophoresis

The phosphate binding affinity of ScPho90 was measured by microscale thermophoresis using a Monolith NT.115 instrument (NanoTemper). ScPho90 (50 nM) was labeled with RED-tris-NTA dye (NanoTemper) in 20 mM HEPES pH 8.0, 100 mM NaCl and 0.005%/0.0005% LMNG/CHS. 10 μL of labeled ScPho90 was mixed with 10 μL of ligand (10 μM–30 mM) in the same buffer. Samples were loaded into premium capillaries (NanoTemper) and MST traces were recorded for 25 s at 25°C with 60% LED power and high MST power. All concentrations were measured in triplicates and normalized fluorescence values at 20 s were used for binding curve analysis.

Negative-stain grid preparation and imaging

SPI Cu, 3mm 400 MESH TEM regular grids were washed in acetone and water initially. A 4 nm carbon layer was produced by a carbon coater (Leica) and gently floated onto the grids. Grids were dried and stored under controlled humanity at room temperature until further use.

Before application of samples grids were glow-discharged using a PELCO easiGlow glow discharger. 3 μL of purified ScPho90 was added on top of the grid and blotted manually using Whatman filter paper. Then 3 μL uranyl formate were added and blotted away

three times. Images were recorded on a Tecnai Spirit microscope operating at 120 kV accelerating voltage and equipped with a Gatan Rio camera. Images were collected manually at a pixel size of 1.2 Å (52,000× magnification) and an exposure time of 3 s using a Gatan Rio camera.

QUANTIFICATION AND STATISTICAL ANALYSIS

Statistical analysis of the transport assays and microscale thermophoresis experiments were done in Origin 2018. Data collection and refinement statistics of the reported cryo-EM data are summarized in Table 1.